Surface Diffusion Manifestation in Electrodeposition of Metal Anodes

Journal:	*Physical Chemistry Chemical Physics*
Manuscript ID	CP-ART-03-2020-001352.R2
Article Type:	Paper
Date Submitted by the Author:	29-Apr-2020
Complete List of Authors:	Vishnugopi, Bairav; Purdue University, School of Mechanical Engineering Hao, Feng; Purdue University, School of Mechanical Engineering Verma, Ankit; Purdue University, School of Mechanical Engineering Mukherjee, Partha; Purdue University, School of Mechanical Engineering

Surface Diffusion Manifestation in Electrodeposition of Metal Anodes

Bairav S. Vishnugopi, Feng Hao, Ankit Verma and Partha P. Mukherjee[*]

School of Mechanical Engineering, Purdue University, West Lafayette, IN 47907, USA

A revised manuscript submitted to

Physical Chemistry Chemical Physics

[*] *Correspondence*: pmukherjee@purdue.edu

Abstract

Metal anode-based battery systems have been deemed indispensable towards energy storage renaissance engendering extensive research into strategies countering dendritic growth of metal electrodeposition. Fundamentally, the morphological evolution of a material is uniquely characterized by the heights of its self-diffusion barrier across multiple pathways. Herein, based on a coarse-grained kinetic Monte Carlo method, we derive insights into the nucleation and growth of metallic electrodeposits in liquid electrolytes, governed by surface self-diffusion characteristics cognizant of the diverse diffusion routes including *terrace, away from step* and *interlayer* pathways. We deconvolve the roles played by each of these surface diffusion mechanisms in conjunction with the electrochemical reaction rate on the deposition morphology regime (film vs mossy vs fractal). We identify interlayer diffusion as the predominant morphology-determining mechanism; dendrite-free deposition even at moderate current rates constrains this diffusion barrier to an upper limit. Additionally, we highlight subtle features amidst the realm of the morphological growth assortment that connect to the cell's electrochemical performance. Finally, we delineate morphological features of Li, Na, Mg and Al based on their respective surface diffusion barriers and applied overpotentials, and provide a baseline for the interpretation of experimental observations. This fundamental study sheds light on the mesoscale underpinnings of morphological variances in mono-valent and multi-valent metal electrodeposition.

Keywords: electrodeposition stability; morphological evolution; surface self-diffusion; interlayer pathways; reaction kinetics; dendrite-free deposits

1. Introduction

As conventional lithium-ion batteries (LIBs) are inching towards their theoretical energy density limits, there has been a resurgence of research focus in exploring battery systems beyond Li-ion chemistry.[1] Emanating from its high theoretical specific capacity (3860 mAh g^{-1}), low density and the lowest electrochemical potential (-3.04 V vs SHE), Li metal has emerged as an attractive anode material.[2-6] Li metal anodes, paired with transitional metal oxide cathodes or novel cathodes based on conversion chemistry (e.g. sulfur, oxygen) promise a significant increase in energy densities compared to current LIBs.[7, 8] They offer a potential pathway to meeting the expanding demands of energy storage and resolving the bottleneck in the commercialization of long-range electric vehicles. However, the realization of such Li-metal-based batteries is confronted by two key challenges: unmitigated growth of dendrites and low Coulombic efficiency, leading to a poor cycle life.[9-12] In addition, the growth of sharp or needle-like dendritic protrusions pose a severe safety threat as they can pierce the pores of the separator, internally short the cell and thereby, lead to catastrophic accidents.[13, 14]

Subsequently, several other metal electrodes like magnesium (Mg),[15-18] sodium (Na),[19-22] potassium (K),[23-25] aluminum (Al)[26, 27] etc. have garnered tremendous attention from researchers. Some of these metals (like Mg, Al) along with offering multi-valence redox benefits, low cost and high abundance, have been interestingly associated with a 'non-dendritic' electrodeposition behavior. This trend has also fostered the application of these metals for air-based batteries[28, 29] and fast charging conditions. Given the critical role of dendrites in battery safety and performance, it is imperative to mechanistically understand the process of electrodeposition and morphology evolution over a wide range of metal electrodes.

Till date, there have been several studies in literature that describe the morphology evolution in electrochemical systems. Dendrite propagation models, developed by Barton and Bockris[30] and Monroe *et al.*[31] explained growth velocity in terms of the surface overpotential and tip curvature. It was concluded that dendrites significantly accelerate across the cells even below limiting current densities, owing to an enhancement of spherical diffusion at their tips. The earliest works demonstrating the effect of adatoms surface diffusion on morphological instability was by Aogaki and Makino leading to the reduction of surface irregularities and suppression of crystal peak growth rates under galvanostatic electrodeposition.[32, 33] In contrast, Chazalviel[34] presented a space-charge model that correlated dendrite propagation purely to ion depletion at the electrode vicinity, thus predicting nucleation and dendrite growth only above limiting current densities. Other continuum level models have been developed to capture the interfacial evolution utilizing phase-field theory[35, 36] and explain the dynamic evolution of voltage and current profiles during electrodeposition.[37, 38] However, these continuum level models do not incorporate element-specific self-diffusion pathways and are thus, relatively agnostic of the electrodeposited metal. They cannot explain the disparities in electrodeposition morphologies that have been observed over different metal electrodes, for instance, the relative lack of dendrite formation of Mg. Recently, Jäckle *et al.* proposed surface self-diffusion barrier as a descriptor for dendrite growth based on the analysis of the barriers of terrace diffusion and across-step diffusion for various metals.[39, 40]

In fact, surface diffusion has been investigated in detail for problems pertaining to phase transformation,[41] crystal growth on catalysts[42] and self-assembly,[43] and regarded as one of the most fundamental phenomena on an active surface,[44-49] governing physical and chemical reactions. Surface self-diffusion of single atoms is of considerable interest, which provides a tractable mechanism for the complex dynamical evolution of crystal surfaces.[46, 47] In earlier studies, field-ion microscopy (FIM) and scanning tunneling microscopy (STM) were used to reveal the nature of self-diffusion at the atomic scale.[50-52] Fundamentally, those pioneering studies have unraveled the hopping and exchange mechanisms of surface self-diffusion,[53-55] the factors affecting self-diffusion,[56-58] and the role of self-diffusion in crystal growth and epitaxy.[59-61] For instance, a rich variety of intriguing geometric patterns manipulated by surface diffusion were captured in experiments, such as fractal islands[62] and compact islands with the shapes of square, triangle, and hexagon.[60, 63] In addition to experiments, theoretical models have been developed to examine the surface self-diffusion effect on crystal growth and surface morphology. Burton *et al.* comprehensively discussed the growth mechanisms based on the terrace-step-kink (TSK) model.[64] Subsequently, Schwoebel and Shipsey built a growth model with the emphasis of step motion,[65] and Zhang *et al.* also systematically investigated the dependence of surface morphology of the energy barrier related to interlayer diffusion.[66] Kardar *et al.* probed the surface evolution of a growing solid film using the nonlinear Langevin equation and established the framework of the kinetic roughening.[67]

In equivalence to solidification and epitaxy, surface self-diffusion could play a critical role in the nucleation and growth of metal electrodes during electrodeposition.[68, 69] As computed in [[39, 40]], a large/small away from the step barrier and a low/high terrace and interlayer (across-step) diffusion barriers of (Mg, Al)/ (Li, Na) intuitively explain their preferred configurations and prove to be an important step towards understanding their proclivity for dendrite formation. However, during electrodeposition, these surface diffusion processes compete with ion transport, reaction at the metal-electrolyte interface and amongst themselves. Therefore, a fundamental understanding of the morphological evolution of metal electrodes, incorporating the various mechanisms of surface diffusion and electrodeposition rate, is needed. The Kinetic Monte Carlo (KMC) approach has proven useful in modeling electrodeposition from atomistic to continuum length/time scales including the mechanisms of diffusion limited aggregation, surface diffusion and metal structural heterogeneities for non-battery systems.[70-73] Consequently, we develop a coarse-grained mesoscale model (KMC) to deconvolve the roles of three different self-diffusion mechanisms (terrace diffusion, diffusion away from a step and interlayer/across-step diffusion) in an appropriate electrochemical environment, with ion transport and reaction at the interface and metal battery specific constraints. Based on our simulations, we identify that terrace diffusion significantly alters the film porosity and nucleation density of island electrodeposits. This affects the formation of solid electrolyte interphase (SEI) and consumption of the electrolyte, explaining observations of increased internal resistance and electrolyte drying. An interesting conclusion is the minimal impact of barrier height for diffusion away from a step on the resultant electrodeposition morphology. On the contrary, interlayer/across-step diffusion plays a pivotal role (especially with increasing reaction rates) in determining the film porosity and the varying nature of deposit morphology from film-like to fractal. Furthermore, this study enables us to provide guidelines for future DFT computations towards effective screening of novel electrode materials. The recent advent of eutectic alloy electrodes (X+Y) that promise dendrite-free electrodeposition has opened up a new strata of next-generation batteries.[21, 74, 75] A fundamental understanding of the co-deposition mechanism, in particular, heterogeneous binary surface diffusion parameters (X on Y/Y on X) is essential towards delineating feasibility for dendrite suppression.

For higher deposition rates, (which are of interest for fast charging conditions), we propose interlayer/across-step diffusion barrier as an innate metal property that can serve as a classifier for dendritic and non-dendritic electrodeposition behavior. Based on the mesoscale model, we develop a morphology map that delineates the maximum barrier height of interlayer diffusion, which can compensate for an increase in the electrochemical reaction rates, to form a film-like morphology. Physically, a sufficiently low across-step diffusion barrier allows atoms to descend from sharp dendrite tips as fast as they get reduced at the corresponding lattice site.

Finally, we delineate the morphological features of Li, Na, Mg and Al electrodes based on their respective surface diffusion barriers. Apart from the anomalous behavior of Al in ionic liquids[76] and Mg from Grignard reagents[16], the computed electrodeposition morphologies show a good agreement with experiments. We examine the electrodeposition stability of these metals at various applied overpotentials and demarcate safety limits for Li and Na, which exhibit dendritic behavior.

2. Methodology

To mimic the phenomenon of electrodeposition, three fundamental processes occurring at the vicinity of the metal electrode have been incorporated in our coarse-grained mesoscale formalism. Metal ions (M^{z+}) transport across the electrolyte domain and reach the electrode surface. Subsequent to their arrival at the reaction front (metal-electrolyte interface), they are reduced upon reaction with an electron. Once deposited, these atoms are not restrained to their reaction sites, and diffuse over the electrode surface. As shown in Fig. 1(a-c), we consider three mechanisms of surface self-diffusion in this study:

1. Terrace diffusion

2. Diffusion away from a step and

3. Across-step or interlayer diffusion (to descend)

A schematic of these processes has been depicted in Fig. 1(a-c), along with a representative energy profile based on the reaction path and diffusion barrier height (E_a) in Fig. 1(d). Unless specifically noted, across-step or interlayer diffusion refers to the process of descending in this work. In principle, the phenomenon of surface diffusion is more convoluted; the aforementioned framework helps us simplify the model to maintain tractability, while ensuring sufficient rigor.

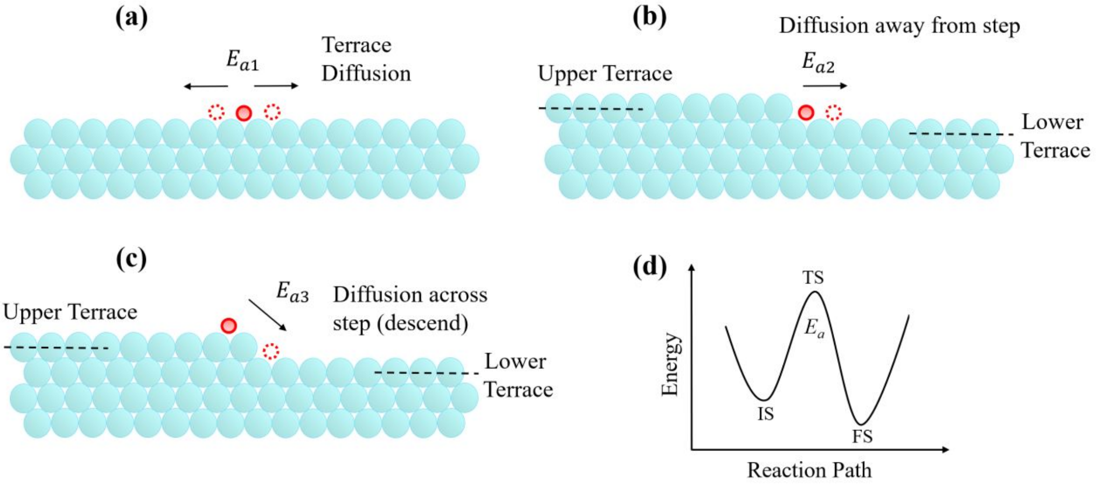

Fig. 1. Schematic of the surface self-diffusion pathways. Surface atoms A, B and C exhibit (a) terrace diffusion (b) diffusion away from a step and (c) interlayer diffusion/diffusion across a step, with energy barriers E_{a1}, E_{a2}, and E_{a3}, respectively. A representative energy profile along the reaction path, showing the initial state (IS), final state (FS), height of the diffusion barrier (E_a) and the transition state (TS) is illustrated in (d).

The principal electrochemical reaction taking place at the reaction front is

$$M^{z+} + ze^{-} \rightarrow M \tag{1}$$

where M atoms are deposited on the electrode surface. The faradaic reaction current density, J, generated due to this reaction is expressed by the Butler-Volmer equation

$$J = i_0\left(exp\left(\frac{\alpha F}{RT}\eta\right) - exp\left(-\frac{\beta F}{RT}\eta\right)\right) \tag{2}$$

Here, α and β are the charge transfer coefficients ($\alpha + \beta = 1$), T is the operating temperature, R is the gas constant, and i_0 is the exchange current density of the charge transfer. η is the local overpotential driving the electrochemical reactions, which is given by

$$\eta = U - U_{eq} \tag{3}$$

where U is the surface potential at the electrode-electrolyte interface and U_{eq} is the equilibrium potential of the reaction.

The surface morphology during electrodeposition evolves based on the competition between ion transport, surface diffusion and electrochemical reaction. These competing phenomena govern morphological features such as shape, size and density of nucleated islands, film porosity and dictate transitions in electrodeposition morphology from stable to mossy and fractal. A distinct aspect of electrodeposition is that ion distribution in the electrolyte affects growth, and growth in turn affects the ion distribution, which is not a feature in epitaxy. The computation of rates corresponding to each of these processes has been described below.

At a single lattice site on the electrode surface, the reaction rate k_L is evaluated as follows

$$k_L = \{0, k_R\} \tag{4}$$

Based on the occupancy of the lattice site at the electrode surface, k_L can assume two possible values: If the lattice site is not occupied by an M^{z+} ion, $k_L = 0$; otherwise $k_L = k_R$, where k_R is the intrinsic reaction rate at the electrode surface, which is given by

$$k_R = \frac{Ja^2}{F} N_a \tag{5}$$

Here, a is the lattice constant and N_a is the Avogadro constant.

Based on the transition state theory[77], surface self-diffusion rate of the electrodeposited atoms is obtained using the Arrhenius equation

$$k_D = \nu \, exp\left(\frac{-E_a}{k_b T}\right) \tag{6}$$

where, ν is the hopping frequency (ranging between $10^{12}\,s^{-1}$ and $10^{13}\,s^{-1}$), k_b is the Boltzmann constant, T is the operating temperature and E_a is the energy barrier (corresponding to the respective mechanism of surface diffusion – see Fig. 1) that deposited atoms need to overcome to diffuse over the electrode surface.

Across the electrolyte domain, M^{z+} ions are assumed to diffuse from one lattice site to a neighboring site. For the sake of computational efficiency, the liquid electrolyte has been replaced by a crystalline structure with the rate constant for ion migration modelled as given below (using values of diffusivity that have been reported in literature[78]).

$$k_T = \frac{D}{d^2} \tag{7}$$

Here, D is the diffusivity of M^+ ions in the electrolyte and d is the distance per diffusion step, given by $d = \sqrt{2}a$.

In this study, we employ a coarse-grained Kinetic Monte Carlo model[79-81] to examine the early stage nucleation and growth of the metal morphology. The 2-D simulation domain consists of 12,000 lattice sites, over a 100×120 grid. A periodic boundary condition is applied along the horizontal direction. The occupation ratio of ions, which physically represents the ratio of the number of M^{z+} ions to the total number of available M^{z+} sites in the electrolyte domain, is set to 2%. In order to enable sustained electrochemical reactions, this value is maintained constant through the addition of new ions to the electrolyte domain from the upper boundary. To obtain the morphologies of Li, Na, Mg and Al (in the later part of the results section), the computation of the occupation ratio (corresponding to $1000\ \mathrm{mol/m^3}$) is synergized based on their respective molar volumes.[82] The electrochemical system is allowed to dynamically evolve until the deposition of 2000 atoms. The Kinetic Monte Carlo modeling approach and the computational algorithm have been explained in detail in the **Supplementary Information**. Unless specifically mentioned, parameters used in the model have been summarized in Table S1. Electrodeposition morphologies obtained based on the Kinetic Monte Carlo method have been classified into three categories, namely film-type, mossy and fractal. Mossy and fractal morphologies have been differentiated based on the the number of branches, number of nuclei on the electrode surface and the height of the electrodeposited structure. When compared to mossy morphologies, fractal morphologies encompass extensively branched structures (usually thinner), greater number of nucleated islands and a larger dendritic height.

3. Results and Discussion

3.1. Surface Diffusion vs Reaction Kinetics

As depicted in Fig. 1, we have considered three mechanisms of surface self-diffusion (terrace, away from a step and across-step/interlayer) in this study. To begin with, we simplify the investigation by examining two ideal scenarios: (1) without interlayer diffusion by setting E_{a1} = 0.15 eV and E_{a2} = 0.3 eV and (2) without diffusion away from a step by setting E_{a1} = 0.15 eV and E_{a3} = 0.3 eV. Here E_{a1}, E_{a2} and E_{a3} refer to the barrier heights of terrace diffusion, diffusion away from a step, and interlayer diffusion, respectively. The electrodeposition morphologies at various applied overpotentials (or deposition rates) for these scenarios have been shown in Fig. 2. As illustrated in Fig. 2 (a), for the first scenario, the growth mode undergoes two morphological transitions with an increase in overpotential, i.e. from film-type to mossy and from mossy to fractal. These morphological transitions emanate from the competition between the surface self-diffusion kinetics and deposition rate.[82] A relatively low deposition rate facilitates adequate surface relaxations before the existing surface gets covered with freshly deposited atoms, and thereby leads to an even surface morphology. However, it is to be noted that the resulting growth front of this film-type electrodeposit exhibits a moderate degree of roughness during its early stage of electrodeposition. At a significantly higher overpotential, reduction of metal ions recurrently occurs on top of deposited atoms, rendering surface diffusion incompetent to it. Furthermore, it leads to a depletion of metal ions in the vicinity of the electrode surface, corresponding to a transport-limited regime. As a consequence of both these effects, growth of initially nucleated islands results in the formation of a dendritic morphology. This phenomenon has been depicted in Fig. S3 of the **Supplementary Information**. From the mechanism depicted in Fig. S3, it can be inferred that since a fundamental mechanism that triggers the onset of dendrites is the depletion of ions at the metal-electrolyte interface, an increase in the electrolyte concentration or an enhancement in the electrolyte transport properties can help alleviate dendrite growth at high overpotentials. As shown in Fig. S3, fractal growth regimes exhibit strong interactions between dendrites, which was not considered for dendrite propagation in previous theoretical studies.[31] It is to be noted that diffusion of deposited atoms along fractals and mossy structures (as shown in Fig. 2(a)) is accounted for in our coarse-grained kinetic Monte Carlo method. Any deposited atom has a probability to diffuse along the surface depending on the activation barrier and the vacant neighboring positions that it can fill in.

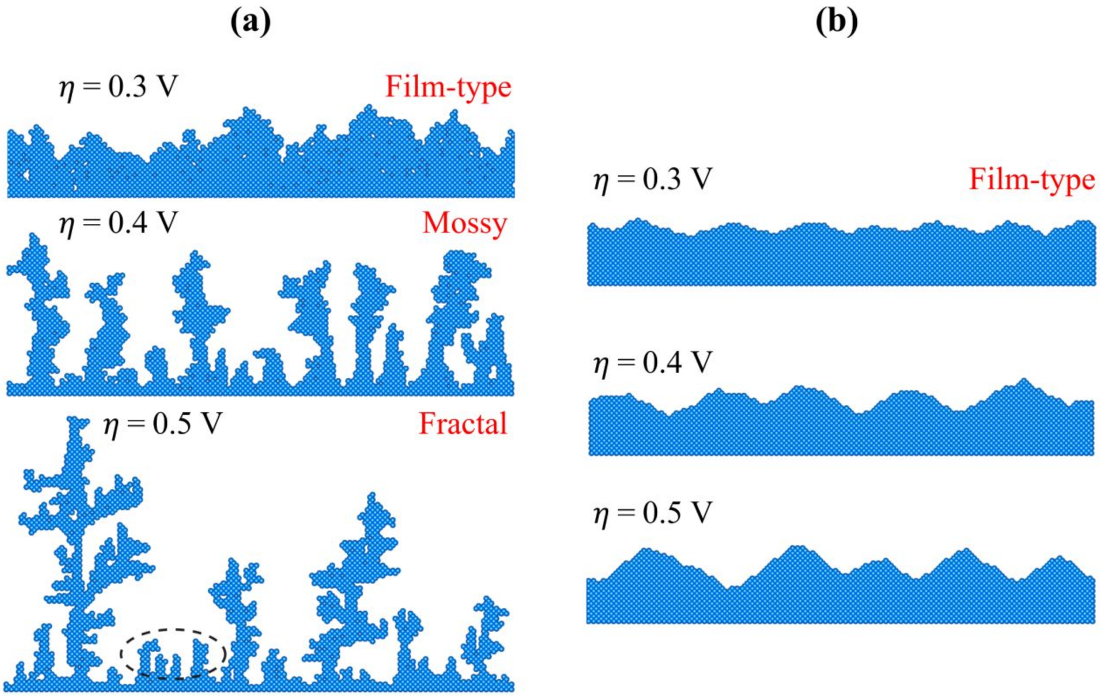

Fig. 2. Electrodeposition morphologies obtained at an overpotential of 0.3 V, 0.4 V and 0.5 V. Two specific conditions are set for the self-diffusion barriers: (a) E_{a1} = 0.15 eV and E_{a2} = 0.3 eV with $E_{a3} \to \infty$; (b) E_{a1}= 0.15 eV and E_{a3} = 0.3 eV with $E_{a2} \to \infty$.

In addition, the density of initial nucleated islands, N, highlighted by the circle in Fig. 2(a), could be related to surface diffusion coefficient D_s and deposition rate F

$$N\,\alpha\,\frac{F^p}{{D_s}^q} \qquad (8)$$

where p and q are positive constants. D_s is related to the surface self-diffusion rate k_T using the expression $D_s = d^2 k_D$, which is given in Equation (6). In comparison to the mossy growth in Fig. 2(a), the fractal growth has a larger island density over the electrode surface, complying with Equation (8).

In contrast to the morphologies in Fig. 2(a), a compact and film-type morphology is favored in Fig. 2(b) regardless of the value of overpotential (in the range of 0.3-0.5 V), albeit exhibiting enhanced surface roughening with increasing overpotential. An extensive relaxation of the metal surface has noticeably stabilized the process of electrodeposition. Simulations of this ideal scenario involved two conditions, strikingly different from the first case: (1) Presence of interlayer diffusion and (2) absence of diffusion away from a step. For interlayer diffusion via an exchange mechanism, a highly coordinated transition state is feasible. This, in turn reduces the diffusion barrier for descending and as per the transition state theory, increases the rate of the process. Physically, this stimulates atoms to migrate from elevated tops to lower terraces, enabling the formation of smoother morphologies. However, it is also possible for atoms deposited aside such a step to migrate away from them. Such an event would lead to a lower coordinated state and foster nucleation of a disjoint island. Theoretically, it is thus preferred to have a low barrier height for interlayer diffusion and a high barrier height for diffusion away from a step. It is apparent from visual inspection of Fig. 2, that a film-type morphology (formed in the second scenario) encompasses highly coordinated atoms, owing to both the presence of interlayer (across-step) diffusion and an absence of diffusion away a step. However, we have still not deconvolved their individual roles, if any, in healing the surface morphology.

The two scenarios investigated above could still be used to qualitatively explain the difference in electrodeposition morphologies formed by Li and Mg. Based on experimental observations, Li tends to form mossy and dendritic morphologies at high deposition rates,[14] while Mg exhibits lower proclivity to dendritic growth.[83] DFT calculations in [40] revealed that Li has a large barrier height for interlayer diffusion (0.4 eV) and a low barrier height for diffusion away from a step (0.3 eV). On the contrary, Mg has a low barrier height for interlayer diffusion (0.01 eV) and a large barrier height for diffusion away from a step (0.62 eV). Thus, the results shown in Fig. 2 are in good agreement with the electrodeposition morphologies of Li and Mg that have been observed experimentally. They also illustrate that transport of single atoms plays a pivotal role in stabilizing metal growth and achieving a uniform deposition layer.

We now deconvolve the implications of each surface diffusion mechanism and probe their competence with the deposition rate at different applied overpotentials. A morphology map, in terms of E_{a1} and E_{a2}, at $\eta = 0.3$ V and $\eta = 0.5$ V is illustrated in Fig. 3. The metal morphology exhibits distinct traits based on the barrier heights of surface diffusion at each of these overpotentials. We begin the analysis by visually inspecting the displayed morphologies at the extremes of both these maps. Theoretically, it is desired to have a low barrier height for terrace diffusion and a large barrier height for diffusion away from a step. Therefore, in both these maps, any improvement in the surface morphology (from the bottom to top corner) can be attributed to an increase in the barrier height for diffusion away from a step, while any deterioration can be attributed to an increase in the barrier height for terrace diffusion. On visual examination, the morphologies do not show any surface smoothening on going from the bottom to top corner at $\eta = 0.3$ V and 0.5 V. Therefore, we conclusively deduce that any adverse impact on the surface morphology is due an increase in the barrier height of terrace diffusion. Additionally, we also infer that an increase in the barrier height for diffusion away from a step proves to have a negligible beneficial impact on the electrodeposition morphology.

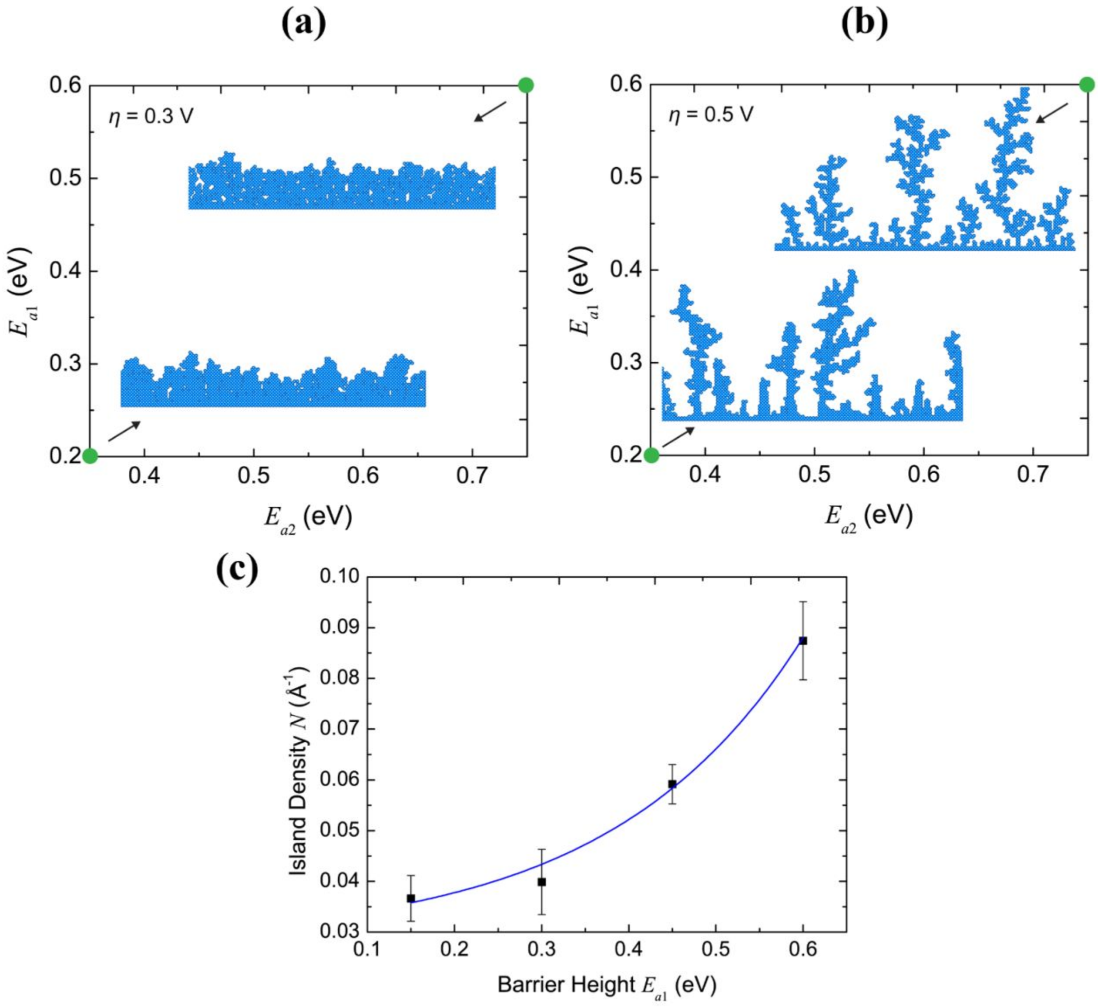

Fig. 3. Morphology maps in terms of terrace diffusion barrier (E_{a1}) and energy barrier of diffusion away from a step (E_{a2}), for an overpotential (η) of 0.3 V in (a) and 0.5 V in (b). (c) Density of initial nucleated islands as a function of E_{a1}, $N = 0.0039 \exp(4.56 E_{a1}) + 0.028$ Å^{-1}, where $E_{a2} = E_{a1} + 0.15$ eV is set.

As shown in Fig. 3(a), at a relatively low deposition rate, the porosity of the film-type metal increases with an increase in the barrier height of terrace diffusion, owing to a sluggish transport of surface atoms. Physically, adatoms are incapable of diffusing to favorable sites before being pinned on the growth front by the arrival of newly deposited atoms. On the other hand, the fractal morphology exhibits two discrete features at a high deposition rate. Firstly, nucleated islands on the electrode surface are not interlinked with each other, thereby impeding the formation of a film-type morphology. As shown in Fig. 3(c), the island density exponentially increases with the height of terrace diffusion barrier. Initially, the deposited single atoms meet and form dimers. For low terrace diffusion barriers, newly deposited atoms will diffuse rapidly on the surface and predominantly fuse with those dimers to form larger islands. On the contrary, sluggish terrace diffusion of atoms facilitates nucleation of new islands, leading to a relatively large island density. Secondly, the branch thickness of the fractal metal is shrunk with decreasing surface diffusion rate, as depicted in Fig. 3(b). This is complementary to the results of a previous study[84] that reported a reduction in branch thickness of Pt from 23 Å to 13 Å. In their study, a reduction in self-diffusion rate was brought about due to a change in temperature from 245 K to 180 K. Physically, a high self-diffusion rate allows an adatom to relax swiftly to an energetically favored site, i.e., the highly coordinated site with more neighbors. As a result, enough local relaxation contributes to widening of the branches. However, based on Fig. 3(a) and Fig. 3(b), we infer that though E_{a1} affects morphological features like porosity, nucleation density and branch thickness, it is unable to alter the nature of the electrodeposition morphology. In other words, the electrodeposit being film-like or fractal depends only on the overpotential or deposition rate in the absence of interlayer diffusion. This inference is further reinforced by our next set of simulations.

A morphology map, combining the three self-diffusion processes is illustrated in Fig. 4, where we set $E_{a2} = E_{a1} + 0.15$ eV. Fig. 4(a) depicts the influence of these processes on the porosity and surface roughness of the film-type morphology at η

$= 0.3$ V. Based on this, we identify that in addition to terrace diffusion, interlayer diffusion plays a crucial role in determining the porosity of the metallic film. At a higher deposition rate, interlayer diffusion exhibits substantial competence, leading to three distinct growth regimes – film-type, mixed and dendritic as shown in Fig. 4(b). Even at a higher deposition rate, it is interesting to note that film-type growth mode is preserved for a low barrier of interlayer diffusion. From the morphology map in Fig. 4(b), we infer that an interlayer barrier of ~ 0.3 eV is capable of compensating for the enhanced rate of electrochemical reaction at $\eta = 0.5$ V. Analogously, lower interlayer barrier heights would be required to form stable deposits at higher overpotentials. As expected, a higher barrier height in Fig. 4(b) results in a dendritic growth regime. Between these two regimes, a mixed growth regime exists, with the co-occurrence of film-type, needle-like, and fractal morphologies.

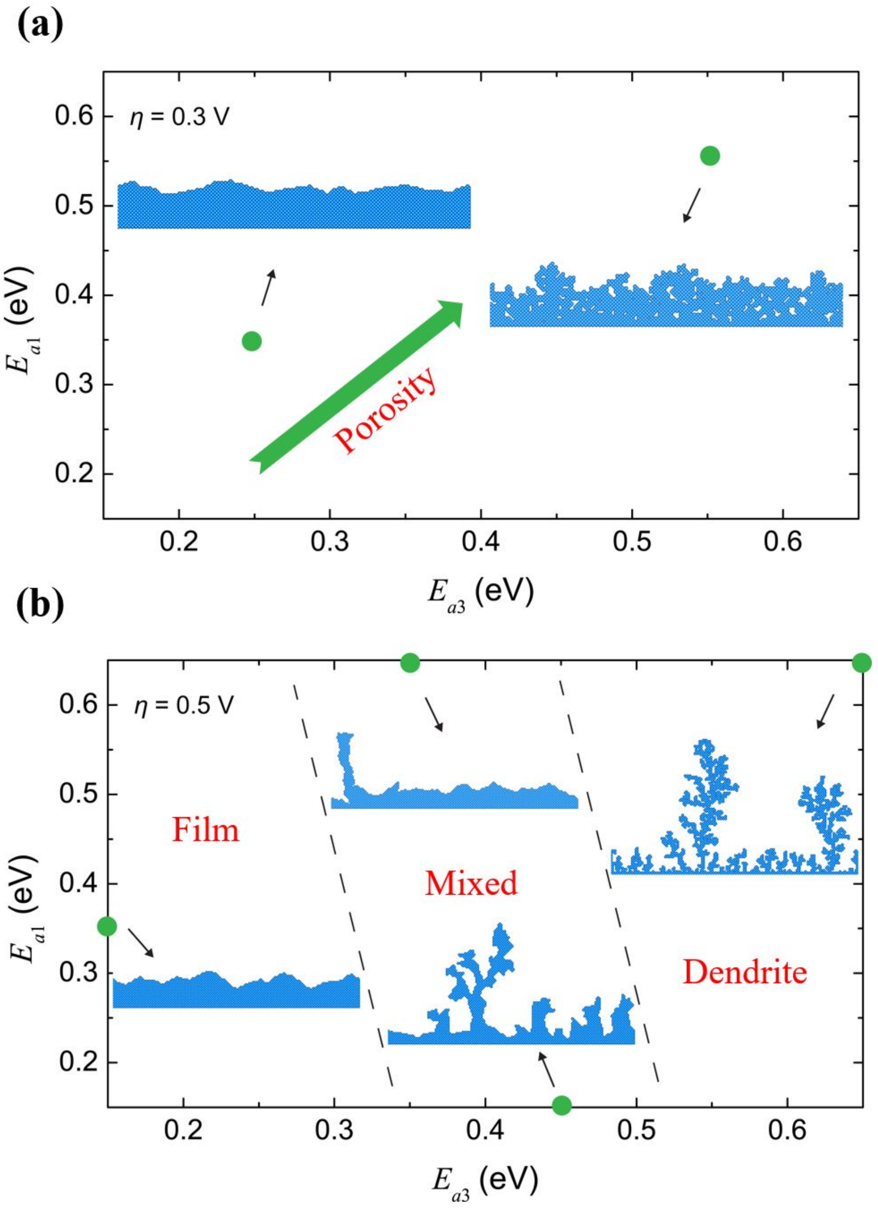

Fig. 4. Phase maps of electrodeposition morphology in terms of terrace diffusion barrier (E_{a1}) and interlayer diffusion barrier (E_{a3}), with the energy barrier of diffusion away from steps set to $E_{a2} = E_{a1} + 0.15$ eV. Overpotential (η) is set 0.3 V in (a) and 0.5 V in (b).

The results indicate that terrace diffusion alters surface reconstruction and influences subtle morphological features like porosity, nucleation density and branch thickness. These changes affect the electrochemical performance of the cell. The presence of pores/voids allow for electrolyte seepage and generation of fresh metal-electrolyte interfaces resulting in consumption of the electrolyte through SEI formation, which in turn causes electrolyte drying and increased internal resistance. The mechanical integrity of the electrode is also compromised if the voids occupy large spaces and subsequent stripping process can result in the formation of dead metal strands. Barrier height for diffusion away from the step shows negligible impact on the morphology. On the contrary, interlayer diffusion barrier influences film porosity and plays a pivotal role in stabilizing the process of electrodeposition. Further, it could serve as a classifier for identifying innate dendritic and non-dendritic proclivity. Dendritic growth modes adversely impact electrochemical performance by stimulating the process of necking and stripping during discharge.[12, 85] Further, based on our mesoscale model, we predict the required barrier height of interlayer diffusion that can facilitate formation of a stable deposit at high overpotentials, $\eta = 0.5$ V, to be below 0.3 eV.

3.2. Case study - Li, Na, Mg & Al metal electrodes

In this section, we aim to delineate the morphological features of Li, Na, Mg and Al metal electrodes based on their respective diffusion barrier heights. We evaluate their electrodeposition stability at various overpotentials and demarcate safety limits, beyond which dendrite growth is inevitably triggered. It is to be noted that though Li and Na are bcc metals, while Mg and Al crystallize in close-packed structures, the same surface morphology have been used for all these metal systems. The barrier heights of the three diffusion mechanisms[40] used to simulate the morphology evolution of these metal electrodes have been summarized in Table 1.

Fig. 5(a) depicts the electrodeposition morphologies of Li at $\eta = 0.6$ V and 0.8 V. A mossy and porous metallic structure is obtained at an overpotential value of 0.6 V. It encompasses small protrusions over its rough surface, which can evolve into distinct pillars. The presence of voids inside the structure are indicative of possible mechanical degradation, electrolyte consumption and electrolyte confinement. Clearly, at $\eta = 0.8$ V, a fractal or dendritic morphology is obtained, owing to the dominance of reaction kinetics over all surface diffusion mechanisms. These dendritic structures contain sharp protrusions that could pierce the separator pores and possibly short the cell. The electrodeposition morphologies of Na, as shown in Fig. 5(b) exhibit improved stabilities at these overpotentials. However, at $\eta = 0.8$ V, small dendritic protrusions begin to emanate over the metal surface. It is to be noted that though the Ehrlich-Schwoebel barrier (which is the difference in the barrier heights of interlayer and terrace diffusion) of Na is only 0.01 eV, it still shows tendency to form dendrites. This dendritic proclivity of Na can thus be attributed to its large values of terrace and interlayer diffusion barriers. Thus, based on our simulations, we obtain a safe overpotential limit of 0.6 V and 0.8 V for Li and Na, above which dendrite growth is triggered.

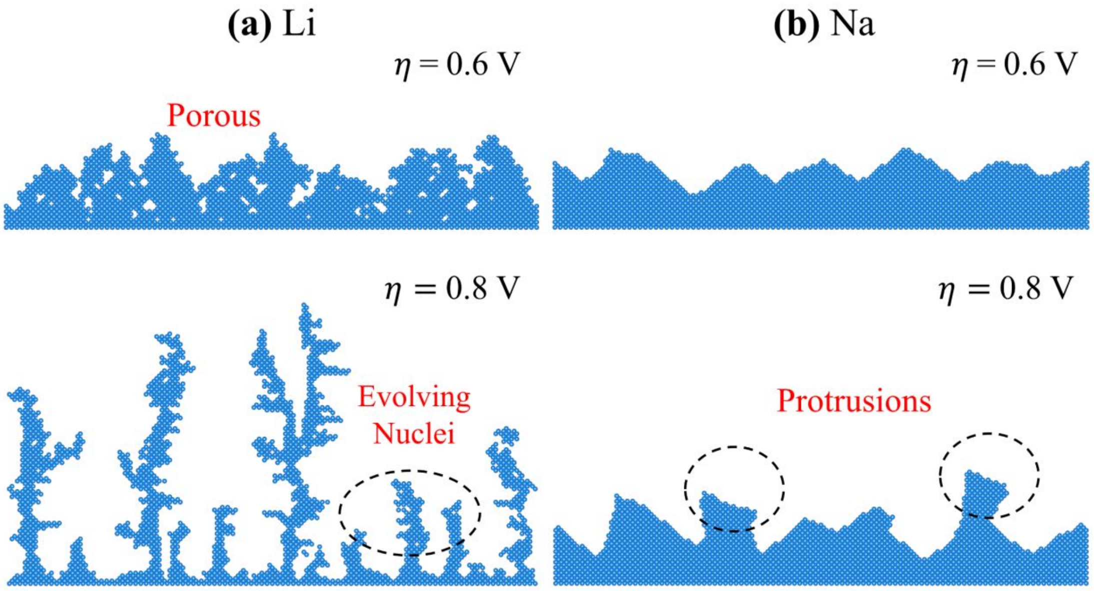

Fig. 5. Electrodeposition morphologies of (a) Li and (b) Na at $\eta = 0.6$ V and 0.8 V.

In contrast to the Li and Na, both Mg and Al exhibit stable electrodeposition morphologies at $\eta = 0.6$ V and 0.8 V. As shown in Fig. 6, they form stable, compact electrodeposits, containing peaks and valleys. This contrasting electrodeposition behavior of Li and Mg (when compared to Li and Na) can be attributed to their low barrier heights of terrace and interlayer diffusion. The morphological features of these metal electrodes along with their respective barrier heights for surface diffusion have been summarized in Table 1. However, this understanding requires further enhancement as both Mg and Al have been reported to show dendritic behavior. As reported in [76] and [16], Al shows tendency to form dendrites in ionic liquids, while Mg dendrites have been observed in Grignard reagents.

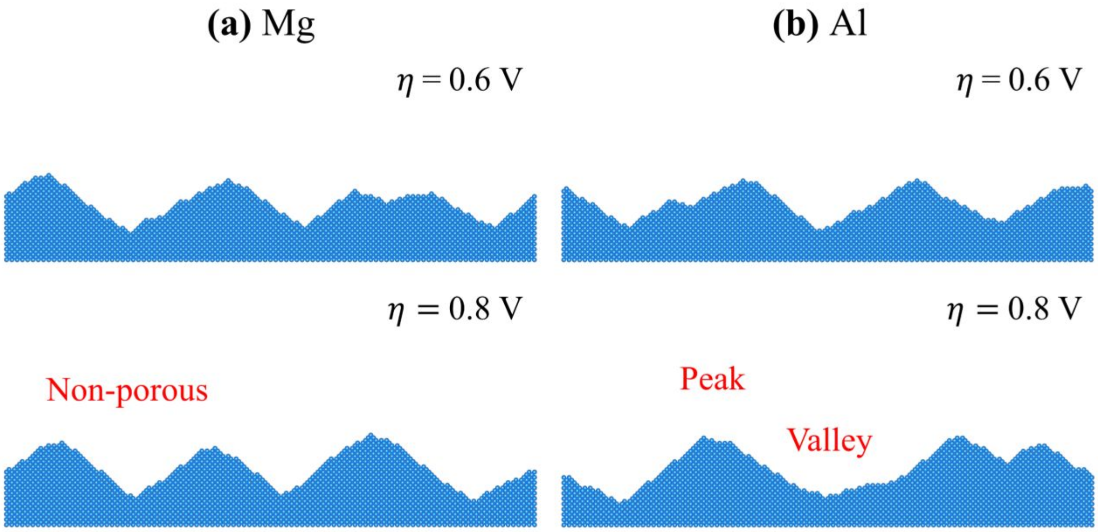

Fig. 6. Electrodeposition morphologies of (a) Mg and (b) Al at $\eta = 0.6$ V and 0.8 V.

Based on the results of the case studies, we infer the following:

1. The tendency of Li to form a porous, rough and mossy structure at moderate reaction rates (η = 0.6 V) hints at possible explanations for its cell failure. Even without dendrites piercing separator pores, electrolyte starvation is imminent due to prolonged adverse SEI formation at the interface of these pores. However, at higher reaction rates (η = 0.8 V), sharp dendritic protrusions (as shown in Fig. 5(a)) render the cells highly prone to a short-circuit.

2. In contrast to Li, our simulations show that Na does not tend to form a porous deposit, eliminating the likelihood of electrolyte consumption and drying. Therefore, its dendritic proclivity can be majorly attributed to the reaction kinetics at the interface, which is dependent on the kinetic overpotential. A review of the experimental findings in [86] sheds light on this phenomenon. It was reported that for the same value of applied current density, Na/Na symmetric cells exhibit larger polarization (and thus larger overpotential values) than Li/Li symmetric cells. This further solidifies our hypothesis

that the dominance of reaction kinetics is a major contributor to Na's dendritic behavior.

To summarize, Li has an inherent tendency to form porous and dendritic structures, irrespective of the kinetic overpotential. However, Na can be pushed into the dendritic regime based on the operating conditions (reaction kinetics). Observations of Na dendrites may thus be attributed to larger polarization of the cells, raising questions on the stability of the SEI layer that is formed on its surface.

3. In contrast to Li and Na, our simulations indicate Mg and Al forms compact deposits, encompassing peaks and valleys, irrespective of the kinetic overpotential. This is because their surface self-diffusion rates (as per the transition state theory) are order of magnitudes higher than Na and Li. We can hypothesize observations of dendrite formation in these systems reported in [16] and [76] to either be a manifestation of surface inhomogeneities induced local reaction spikes or extreme long-range transport limitations.

Table 1. Diffusion barrier heights & morphological features for the various metal electrodes

Metal	Barrier Height (eV)			Morphological Features
	Terrace Diffusion	Diffusion away from a step	Interlayer Diffusion	
Li	0.14	0.3	0.4	Porous, rough and mossy surface formed at $\eta = 0.6$ V; fractal morphology formed at η

				$= 0.8$ V.
Na	0.16	-	0.15	Stable electrodeposition at $\eta = 0.6$ V; emergence of dendritic protrusions at $\eta = 0.8$ V
Mg	0.02	0.62	0.01	Compact, Film-like Deposits encompassing peaks and valleys (Exception: [76])
Al	0.05	-	0.06	Compact, Film-like Deposits encompassing peaks and valleys (Exception: [16])

Lastly, it is be noted that in principle, the phenomenon of dendrite growth occurring in metal-based batteries is three-dimensional in nature. However, the kinetic Monte Carlo model developed in the current study is two-dimensional. Consequently, three-dimensional features of the evolving electrodeposit have not been captured, which is a limitation of the current study. Two-dimensional Monte Carlo simulations[87] in the past have been used to investigate features like island densities (relevant to homoepitaxial growth) as explored in our current work; however, developing a three-dimensional model for electrodeposition would provide a deeper understanding of the growth phenomenon and morphological attributes. Subtle features of the morphology like porosity, branch structures and nucleation patterns can be captured with greater precision than with the current two-dimensional model. In addition, mechanical strength of the dendritic structures, which has been excluded in the current study can also be evaluated in a rigorous manner. As part of our future work, a three-dimensional Monte Carlo model to capture the characteristics will be developed.

4. Conclusion

In summary, we developed a coarse-grained mesoscale formalism to investigate the interplay of surface diffusion and reaction kinetics in governing the morphological evolution during electrodeposition. We delineate the contributions of three surface diffusion mechanisms (terrace diffusion, diffusion away from a step and interlayer diffusion) towards the resultant electrodeposition morphology. It is observed that as the deposition rate increases, the growth mode of metal undergoes two transitions when the interlayer diffusion is negligible, i.e., from film-type to mossy and from mossy to dendritic. In contrast, the introduction of interlayer diffusion smoothens the surface, leading to film-type deposition even with increasing electrochemical reaction rates. Based on the morphology map coupling the three mechanisms, we identify the maximum barrier height of interlayer diffusion that can still result in the formation of such a film-like morphology to be around 0.3 eV. Finally, we performed a case study of Li, Na, Mg and Al electrodes, describing their characteristic morphological features at different deposition rates. This study provides the underlying physical mechanisms of morphological evolution during electrodeposition and underscores the importance of enhanced interlayer transport of single atoms for dense film-type deposition. We decipher the rules governing morphological instability of the growth front, shedding light on the principles to tailor deposition morphology from inherent surface properties.

In our current work the effect of solid electrolyte interphase (SEI) has been neglected. In practice, the environment around the growth front, such as the electrolyte and SEI, could affect the kinetics of surface diffusion. In addition, self-heating of the metallic surface has been reported to heal dendrites and substantially smooth the surface, owing to extensively triggered surface diffusion.[88] Therefore, a more comprehensive understanding is required, incorporating these factors. This will be considered in a new mesoscale formulation, as part of our future work.

The current study enables us to provide the following qualitative and quantitative perspectives:

1. Electrochemical performance of the metal battery is crucially influenced by the terrace and interlayer diffusion barriers with the former affecting the film porosity and latter influencing both porosity and the transition from film to dendritic morphology.
2. Even for a moderate current operation with overpotentials ~ 0.5 V, an interlayer diffusion barrier that is limited to ~ 0.3 eV is paramount towards effective dendrite suppression.
3. A theoretical understanding of co-deposition in binary (n=2) alloy systems (for example Li-Na) requires the estimation of $n^2 = 4$ surface diffusion barriers for each diffusion pathway (for example Li on Li, Li on Na, Na on Li and Na on Na). Keeping in mind that DFT computations of barrier heights are expensive with significant running time, cogent dendrite suppression predictions can be made through estimation of the 4 interlayer diffusion barriers only. Furthermore, we propose that barrier height calculations through DFT should focus on getting estimates for interlayer diffusion and terrace diffusion, in that order, with the latter being computed only when all interlayer diffusion barriers are < 0.3 eV.

Conflicts of interest

There are no conflicts to declare.

Author Contributions

BSV and FH contributed equally to this work.

Acknowledgements

The information, data, or work presented herein was funded in part by the Office of Energy Efficiency and Renewable Energy (EERE), U.S. Department of Energy, under Award DE-EE0007766.

References

1. J. W. Choi and D. Aurbach, *Nature Reviews Materials*, 2016, **1**, 16013.
2. X.-B. Cheng, R. Zhang, C.-Z. Zhao and Q. Zhang, *Chemical reviews*, 2017, **117**, 10403-10473.
3. N. Nitta, F. Wu, J. T. Lee and G. Yushin, *Materials today*, 2015, **18**, 252-264.
4. Y. Guo, H. Li and T. Zhai, *Advanced Materials*, 2017, **29**, 1700007.
5. D. Lin, Y. Liu and Y. Cui, *Nature nanotechnology*, 2017, **12**, 194.
6. W. Xu, J. Wang, F. Ding, X. Chen, E. Nasybulin, Y. Zhang and J.-G. Zhang, *Energy & Environmental Science*, 2014, **7**, 513-537.
7. P. G. Bruce, L. J. Hardwick and K. Abraham, *MRS bulletin*, 2011, **36**, 506-512.
8. K. G. Gallagher, S. Goebel, T. Greszler, M. Mathias, W. Oelerich, D. Eroglu and V. Srinivasan, *Energy & Environmental Science*, 2014, **7**, 1555-1563.
9. J. Steiger, D. Kramer and R. Mönig, *Electrochimica Acta*, 2014, **136**, 529-536.
10. J. Steiger, D. Kramer and R. Mönig, *Journal of Power Sources*, 2014, **261**, 112-119.
11. D. Aurbach, E. Zinigrad, Y. Cohen and H. Teller, *Solid state ionics*, 2002, **148**, 405-416.
12. K.-H. Chen, K. N. Wood, E. Kazyak, W. S. LePage, A. L. Davis, A. J. Sanchez and N. P. Dasgupta, *Journal of Materials Chemistry A*, 2017, **5**, 11671-11681.
13. M. Rosso, C. Brissot, A. Teyssot, M. Dollé, L. Sannier, J.-M. Tarascon, R. Bouchet and S. Lascaud, *Electrochimica Acta*, 2006, **51**, 5334-5340.
14. P. Bai, J. Li, F. R. Brushett and M. Z. Bazant, *Energy & Environmental Science*, 2016, **9**, 3221-3229.
15. G. Pandey, R. Agrawal and S. Hashmi, *Journal of Physics and Chemistry of Solids*, 2011, **72**, 1408-1413.
16. R. Davidson, A. Verma, D. Santos, F. Hao, C. Fincher, S. Xiang, J. Van Buskirk, K. Xie, M. Pharr and P. P. Mukherjee, *ACS Energy Letters*, 2018, **4**, 375-376.
17. J. Muldoon, C. B. Bucur, A. G. Oliver, T. Sugimoto, M. Matsui, H. S. Kim, G. D. Allred, J. Zajicek and Y. Kotani, *Energy & Environmental Science*, 2012, **5**, 5941-5950.
18. X. Sun, L. Blanc, G. M. Nolis, P. Bonnick, J. Cabana and L. F. Nazar, *Chemistry of Materials*, 2017, **30**, 121-128.
19. Z. W. Seh, J. Sun, Y. Sun and Y. Cui, *ACS central science*, 2015, **1**, 449-455.
20. Q. Shi, Y. Zhong, M. Wu, H. Wang and H. Wang, *Angewandte Chemie*, 2018, **130**, 9207-9210.
21. Q. Zhang, Y. Lu, L. Miao, Q. Zhao, K. Xia, J. Liang, S. L. Chou and J. Chen, *Angewandte Chemie International Edition*, 2018, **57**, 14796-14800.

22. B. Lee, E. Paek, D. Mitlin and S. W. Lee, *Chemical reviews*, 2019, **119**, 5416-5460.
23. N. Xiao, W. D. McCulloch and Y. Wu, *Journal of the American Chemical Society*, 2017, **139**, 9475-9478.
24. X. Ren and Y. Wu, *Journal of the American Chemical Society*, 2013, **135**, 2923-2926.
25. Y. Liu, Z. Tai, Q. Zhang, H. Wang, W. K. Pang, H. K. Liu, K. Konstantinov and Z. Guo, *Nano Energy*, 2017, **35**, 36-43.
26. J. Jiang, H. Li, J. Huang, K. Li, J. Zeng, Y. Yang, J. Li, Y. Wang, J. Wang and J. Zhao, *ACS applied materials & interfaces*, 2017, **9**, 28486-28494.
27. M.-C. Lin, M. Gong, B. Lu, Y. Wu, D.-Y. Wang, M. Guan, M. Angell, C. Chen, J. Yang and B.-J. Hwang, *Nature*, 2015, **520**, 324.
28. D. Egan, C. P. De León, R. Wood, R. Jones, K. Stokes and F. Walsh, *Journal of Power Sources*, 2013, **236**, 293-310.
29. T. Zhang, Z. Tao and J. Chen, *Materials Horizons*, 2014, **1**, 196-206.
30. J. Barton and J. O. M. Bockris, *Proceedings of the Royal Society of London. Series A. Mathematical and Physical Sciences*, 1962, **268**, 485-505.
31. C. Monroe and J. Newman, *Journal of The Electrochemical Society*, 2003, **150**, A1377-A1384.
32. R. Aogaki and T. Makino, *Journal of The Electrochemical Society*, 1984, **131**, 40-46.
33. R. Aogaki and T. Makino, *Journal of The Electrochemical Society*, 1984, **131**, 46-51.
34. J.-N. Chazalviel, *Physical review A*, 1990, **42**, 7355.
35. Z. Hong and V. Viswanathan, *ACS Energy Letters*, 2018, **3**, 1737-1743.
36. Z. Hong and V. Viswanathan, *ACS Energy Letters*, 2019, **4**, 1012-1019.
37. J. Diggle, A. Despic and J. M. Bockris, *Journal of The Electrochemical Society*, 1969, **116**, 1503-1514.
38. J. Elezgaray, C. Léger and F. Argoul, *Journal of the Electrochemical Society*, 1998, **145**, 2016-2024.
39. M. Jäckle and A. Groß, *The Journal of chemical physics*, 2014, **141**, 174710.
40. M. Jäckle, K. Helmbrecht, M. Smits, D. Stottmeister and A. Groß, *Energy & Environmental Science*, 2018, **11**, 3400-3407.
41. Y. Li, H. Chen, K. Lim, H. D. Deng, J. Lim, D. Fraggedakis, P. M. Attia, S. C. Lee, N. Jin and J. Moškon, *Nature materials*, 2018, **17**, 915.
42. S. Hofmann, G. Csanyi, A. Ferrari, M. Payne and J. Robertson, *Physical review letters*, 2005, **95**, 036101.
43. S. Woo and P. W. Rothemund, *Nature communications*, 2014, **5**, 4889.
44. M. J. Skaug, J. N. Mabry and D. K. Schwartz, *Journal of the American Chemical Society*, 2013, **136**, 1327-1332.
45. K. Wang, C. Zhang, M. Loy and X. Xiao, *Physical review letters*, 2005, **94**, 036103.
46. A. Pimpinelli and J. Villain, *Physics of Crystal Growth, by Alberto Pimpinelli and Jacques Villain, pp. 400. ISBN 0521551986. Cambridge, UK: Cambridge University Press, February 1999.*, 1999, 400.
47. T. Michely and J. Krug, *Islands, mounds and atoms*, Springer Science & Business Media2012.
48. L. Zhu, C. Brian, S. Swallen, P. Straus, M. Ediger and L. Yu, *Physical Review Letters*, 2011, **106**, 256103.
49. C. Zaum and K. Morgenstern, *Physical review letters*, 2018, **121**, 185901.
50. G. Antczak and G. Ehrlich, *Surface science reports*, 2007, **62**, 39-61.
51. G. Ehrlich and F. Hudda, *The Journal of Chemical Physics*, 1966, **44**, 1039-1049.
52. Y. Mo, J. Kleiner, M. Webb and M. Lagally, *Physical review letters*, 1991, **66**, 1998.
53. G. Kellogg and P. J. Feibelman, *Physical review letters*, 1990, **64**, 3143.
54. T. R. Linderoth, S. Horch, E. Lægsgaard, I. Stensgaard and F. Besenbacher, *Physical review letters*, 1997, **78**, 4978.
55. T. T. Tsong, *Progress in surface science*, 2001, **67**, 235-248.
56. J. Hannon, C. Klünker, M. Giesen, H. Ibach, N. Bartelt and J. Hamilton, *Physical review letters*, 1997, **79**, 2506.

57. S. Horch, H. Lorensen, S. Helveg, E. Lægsgaard, I. Stensgaard, K. W. Jacobsen, J. K. Nørskov and F. Besenbacher, *Nature*, 1999, **398**, 134.
58. R. Van Gastel, E. Somfai, S. Van Albada, W. Van Saarloos and J. Frenken, *Physical review letters*, 2001, **86**, 1562.
59. T. Ohta, N. C. Bartelt, S. Nie, K. Thürmer and G. Kellogg, *Physical Review B*, 2010, **81**, 121411.
60. T. Michely, M. Hohage, M. Bott and G. Comsa, *Physical review letters*, 1993, **70**, 3943.
61. J. Evans, P. Thiel and M. C. Bartelt, *Surface science reports*, 2006, **61**, 1-128.
62. H. Röder, E. Hahn, H. Brune, J.-P. Bucher and K. Kern, *Nature*, 1993, **366**, 141.
63. X. Xia, S. Xie, M. Liu, H.-C. Peng, N. Lu, J. Wang, M. J. Kim and Y. Xia, *Proceedings of the National Academy of Sciences*, 2013, **110**, 6669-6673.
64. W.-K. Burton, N. Cabrera and F. Frank, *Philosophical Transactions of the Royal Society of London. Series A, Mathematical and Physical Sciences*, 1951, **243**, 299-358.
65. R. L. Schwoebel and E. J. Shipsey, *Journal of Applied Physics*, 1966, **37**, 3682-3686.
66. Z. Zhang, J. Detch and H. Metiu, *Physical Review B*, 1993, **48**, 4972.
67. M. Kardar, G. Parisi and Y.-C. Zhang, *Physical Review Letters*, 1986, **56**, 889.
68. Y. Ozhabes, D. Gunceler and T. Arias, *arXiv preprint arXiv:1504.05799*, 2015.
69. N. M. Schneider, J. H. Park, J. M. Grogan, D. A. Steingart, H. H. Bau and F. M. Ross, *Nature communications*, 2017, **8**, 2174.
70. M. Castro, R. Cuerno, A. Sánchez and F. Domínguez-Adame, *Physical Review E*, 2000, **62**, 161.
71. T. Treeratanaphitak, M. D. Pritzker and N. M. Abukhdeir, *Electrochimica Acta*, 2014, **121**, 407-414.
72. T. Treeratanaphitak, M. D. Pritzker and N. M. Abukhdeir, *Electrochemistry Communications*, 2014, **46**, 140-143.
73. F. A. Reis, D. di Caprio and A. Taleb, *Physical Review E*, 2017, **96**, 022805.
74. J.-l. Ma, F.-l. Meng, Y. Yu, D.-p. Liu, J.-m. Yan, Y. Zhang, X.-b. Zhang and Q. Jiang, *Nature chemistry*, 2019, **11**, 64.
75. H. Liu, X.-B. Cheng, J.-Q. Huang, S. Kaskel, S. Chou, H. S. Park and Q. Zhang, *ACS Materials Letters*, 2019, **1**, 217-229.
76. D. Pradhan and R. G. Reddy, *Metallurgical and Materials Transactions B*, 2012, **43**, 519-531.
77. G. H. Vineyard, *Journal of Physics and Chemistry of Solids*, 1957, **3**, 121-127.
78. L. O. Valøen and J. N. Reimers, *Journal of The Electrochemical Society*, 2005, **152**, A882-A891.
79. A. F. Voter, in *Radiation effects in solids*, Springer2007, pp. 1-23.
80. F. Hao, A. Verma and P. P. Mukherjee, *ACS applied materials & interfaces*, 2018, **10**, 26320-26327.
81. F. Hao, A. Verma and P. P. Mukherjee, *Journal of Materials Chemistry A*, 2019, **7**, 18442-18450.
82. F. Hao, A. Verma and P. P. Mukherjee, *Energy Storage Materials*, 2019.
83. C. B. Bucur, T. Gregory, A. G. Oliver and J. Muldoon, *The journal of physical chemistry letters*, 2015, **6**, 3578-3591.
84. M. Hohage, M. Bott, M. Morgenstern, Z. Zhang, T. Michely and G. Comsa, *Physical review letters*, 1996, **76**, 2366.
85. K. N. Wood, E. Kazyak, A. F. Chadwick, K.-H. Chen, J.-G. Zhang, K. Thornton and N. P. Dasgupta, *ACS central science*, 2016, **2**, 790-801.
86. D. Iermakova, R. Dugas, M. Palacín and A. Ponrouch, *Journal of The Electrochemical Society*, 2015, **162**, A7060-A7066.
87. P. Ruggerone, A. Kley and M. Scheffler, *Progress in Surface Science*, 1997, **54**, 331-340.
88. L. Li, S. Basu, Y. Wang, Z. Chen, P. Hundekar, B. Wang, J. Shi, Y. Shi, S. Narayanan and N. Koratkar, *Science*, 2018, **359**, 1513-1516.